PCCP

PAPER

Check for updates

Cite this: *Phys. Chem. Chem. Phys.*, 2023, **25**, 19666

Broadband plasmon-induced transparency to an anapole mode induced absorption conversion Janus metastructure by a waveguide structure in the terahertz region

Si Ying Li, Zhao Tang, Di Di Zhu and Hai Feng Zhang *

Received 7th May 2023,
Accepted 30th June 2023

DOI: 10.1039/d3cp02083e

rsc.li/pccp

A Janus metastructure (MS) assisted by a waveguide structure (WGS) resting on anapole modes and exhibiting direction-dependent behavior has been developed in the terahertz (THz) region. Ultra-broadband absorption is formed by the destructive interference through the anapole as well as Janus trait and is shaped by nested WGS. In this design, vanadium dioxide (VO_2) is expected to attain functional transformation from plasmon-induced transparency (PIT) to absorption. The insulating nature of the VO_2 results in the creation of the PIT, which is characterized by a wide and high transmission window ranging from 1.944 THz to 2.284 THz, corresponding to the relative bandwidth of 7.4% above 0.9. However, when the VO_2 reaches the metallic state, a high absorptivity of 0.921 at 2.154 THz can be implemented in the $-z$-direction owing to the excitement of the toroidal dipole and electric dipole moments in the near-infrared region. And in the $+z$-direction, the broadband absorption above 0.9 in the 1.448–2.497 THz range takes shape in virtue of surface plasmon polariton modes, in which intensely localized oscillation of free electrons is confined to the metal–dielectric interface supported by the WGS. Noting that the MS is equipped with a favorable sensitivity to the incidence angle, we develop an ultra-broadband backward absorption in the TM mode from 0.7–10 THz nearly all above 0.9 when the incidence angle changes from 30°–70°. Moreover, owing to the highly symmetrical structure, the MS exhibits exotic polarization angular stability. All the awesome properties make this MS a good candidate for various applications such as in electromagnetic wave steering, spectral analysis, and sensors.

1. Introduction

The terahertz (THz) band is commonly defined as electromagnetic (EM) waves with a frequency between 0.1 and 10 THz. This range has gained significant attention due to its unique spectral characteristics.[1–3] In particular, the development of metastructures (MSs) has become increasingly urgent for effective THz applications. MSs are artificial structures that exhibit unconventional physical properties, including negative permittivity,[4] negative magnetic permeability,[5] and photonic band gap,[6] which make the MSs a popular research topic in academia.

Electronically induced transparency (EIT) is a quantum interference effect based on a three-energy atomic system, which is achieved by generating sharp transmission windows within a wide reflection or absorption band. It is expected to be useful in communication,[7] photonic storage, photonic conversion,[8] and high-sensitivity sensors.[9] Despite its usefulness, the practical applications of EIT have been limited by specific and stringent environmental requirements for atomic-quantum interference formation, which has hindered the miniaturization of EIT devices. However, recent advancements in MS technology have broken the bottleneck of EIT development. Analogues of EIT-like phenomena in plasmonic metamaterials in normal environments have been designed and investigated in recent years. Na *et al.*, for instance, demonstrated the first EIT-like effect in optical MSs, consisting of a gold bar on two symmetric gold wires.[10] Plasmon-induced transparency (PIT) is a phototropic oscillation of free electrons at the interface between a metal and dielectric, exhibiting strong optical confinement. Numerous applications have been proposed so far.[11–13] Bright modes, which show strong coupling with the incident EM field, are distinguished from dark modes that cannot be coupled directly by the external field but can be excited by bright modes through interference coupling.[14] In particular, the quasi-dark mode is capable of being directly excited by the incident EM field, but can only partially couple the incident field energy.

College of Electronic and Optical Engineering & College of Flexible Electronics (Future Technology), Nanjing University of Posts and Telecommunications, Nanjing, 210023, China. E-mail: hanlor@163.com, hanlor@njupt.edu.cn

 This journal is © the Owner Societies 2023

Generated by an induced magnetic dipole (MP) connected in a head-to-tail fashion,[15] a toroidal dipole (TP) was first presented by Zel'Dovich.[16] In 2010, the realization of the TP using four split-ring resonators was experimentally confirmed at microwave frequencies.[17] On the other hand, anapole was introduced as a configuration of destructive interference produced when the amplitude and phase of the TP and the electric dipole (EP) satisfy certain conditions. This configuration can confine the EM field within the scattering source and eliminate it outside the structure, making it an appealing candidate for use in various areas such as nanolasers,[18] absorbers,[19] and high harmonic generation.[20]

Recently, MSs with a judiciously engineered nanostructure (Janus) have been considered a popular notion for controlling light. The broken out-of-plane symmetry of the structures leads to different performances for opposite propagation directions, exhibiting direction-dependent versatile functionalities. The concept was first proposed by scientists at University College London and has since received widespread attention.[21] By precisely controlling the properties of the materials at the nanoscale, Janus MSs can achieve highly controllable EM wave modulation, including wavelength selection, polarization control,[22] and beam manipulation.[23] Surface plasmon polariton modes (SSPPs) are a type of surface plasmon that can be generated on a metal–dielectric interface with properly designed subwavelength structures. SSPPs have attracted widespread attention on account of their unique features,[24] such as low loss, strong confinement, and tunability, which make them fit for various applications in the fields of sensing,[25] imaging, and communications.[26] Based on the Janus MSs, the arrival of SSPPs prompts a fabulous plan for absorber devices.[27–34] The plasmonic absorber driven by SSPPs offers numerous benefits over the planar metamaterial absorber. For example, it can promote customized absorption bandwidth and ultrawideband absorption, as has been demonstrated in previous studies.[35–38] In 2021, Zhu *et al.* proposed an absorptive frequency selective surface, which was supported by a transmission-absorption integrated design *via* the dispersion engineering of SSPPs.[39] Combining SSPPs with Janus MSs can achieve more efficient control of EM waves, with wide-range applications in fields such as optical communications, biomedical sensing, and spectral analysis.

In this work, a Janus MS equipped with a transformation from broadband PIT to the absorption excited by anapole response is provided. In a bid to induce the PIT phenomenon, two metal resonators separated by a certain distance in the dielectric cavity are designed. The MS develops a broadband PIT by the near-field coupling between the localized plasmon resonance and the notched rectangle (NR) as a bright plasmon resonator and cross-shaped (CS) as a quasi-dark plasmon resonator, creating a wide transparent window covering from 2.052 to 2.220 THz with 7.4% relative bandwidth above 0.9. For the formation of the absorption, the four dumbbell-shaped pore (FDSP) structures made of vanadium dioxide (VO_2) were added, giving birth to EPs and TPs. At the provided frequency, EP moments **P** and TP moments **T** show comparable amplitudes but opposite directions. This creates destructive interference, triggering strongly confining fields near the source and minimal emissions in the far-field region. Thus an absorption peak is generated under the joint action of EPs and TPs when VO_2 works. Besides, we further improve the structure through the synergy of SSPPs developed by the WGS. In contrast to previous works, our design is inspired by the directional Janus MSs and exhibits distinctive properties. Specifically, the MS implements a high absorptivity of 0.921 at 2.154 THz in the forward direction ($-z$-direction) and an efficiency of over 0.9 in the frequency range of 1.448–2.497 THz in the backward direction ($+z$-direction), thus achieving frequency selectivity with different effects in the forward and backward directions of EM waves. Furthermore, we provide the analysis of the local electric field and magnetic field to illustrate the mechanism of the MS. Notably, the given MS has excellent polarization insensitivity and incident angle selectivity. As the incident angle is 30°–70°, an ultra-broadband backward absorption from 0.7–10 THz almost all above 0.9 is formed. These distinguished characteristics promise numerous potential applications, including EM compatibility, radar stealth technology, and control of full-space EM waves. Advanced nanofabrication techniques, such as electron beam, ion beam etching, laser printing, sputtering deposition, and self-assembly can be used to fabricate the MSs. Several experiments have been conducted as reported in ref. 40 and 42. And the manufacturing process for the design can follow the steps described in ref. 40–43. In this paper, we focus on methodological innovation, and the experiment is not followed up at the moment.

2. Design process and discussion

2.1 Theoretical model

Fig. 1 and 2 present a three-dimensional (3D) view and schematic diagrams of the proposed MS. The MS is composed of three nested layers, with the first layer utilizing two additional metal resonators to induce the EIT phenomenon. The NR and CS metal sheet are made of gold with a conductivity of 4.561×10^7 S m^{-1} [44] and a thickness of 0.05 μm as described in Fig. 2(a) and (c). They are positioned opposite to each other on the front side of a dielectric substrate consisting of polyimide, which is characterized by a dielectric constant of 3.5 and a loss angle of 0.003.[45] Additionally, the FDSP structures made of tunable VO_2 are laid in front of the NR. VO_2 can transition from an insulator to a conductor with changes in ambient temperature, electric field, and light intensity. And we will discuss the state switching as the VO_2's conductivity changes from 10 S m^{-1} to 3×10^5 S m^{-1} with the dielectric constant and permeability being both 1.[46] As presented in Fig. 1(b), the size of each layer of the FDSP is the same as that of the dielectric substrate, in the sequence of side lengths with a_1, a_2, and a_3. For the sake of simplicity and aesthetics, only the FDSP of the first layer structure is provided. Unfolding the side and intermediate layers of the first layer structure in Fig. 2(e) yields Fig. 2(d) and (f), in which the thickness of each element is clearly shown. The intermediate layer structure

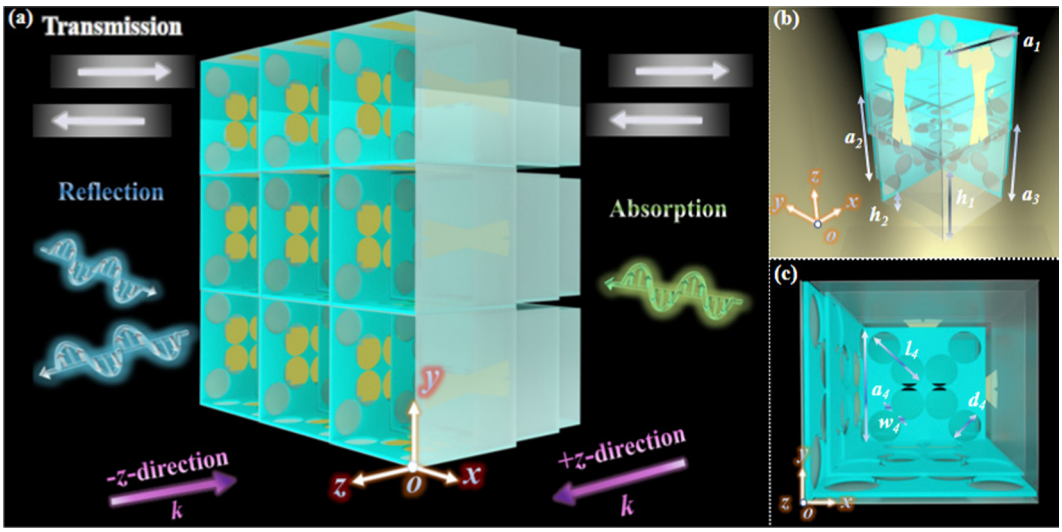

Fig. 1 (a) The periodic array of the MS and illustrations for its major behaviors. (b) Structure diagram of the MS. (c) The front view of the design.

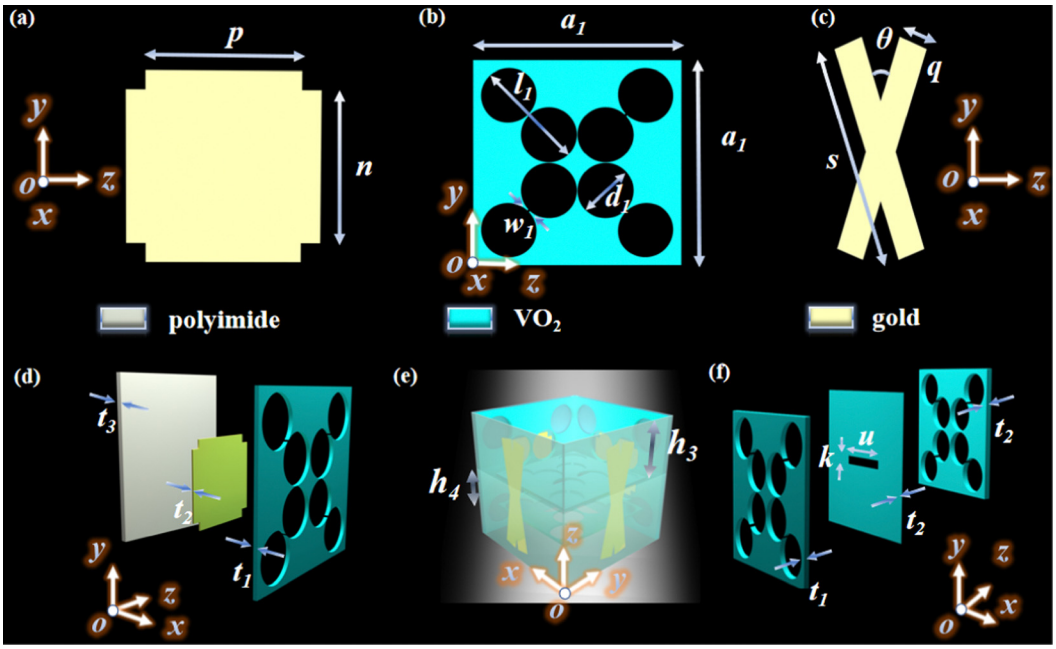

Fig. 2 (a) The front view of the NR. (b) The front view of the FDSP. (c) The front view of the CS. (d) The left side unfolding view of the first layer of the MS. (e) Structure diagram of the first layer of the MS. (f) The right side unfolding view of the first layer of the MS.

in Fig. 2(f) is formed of two identical FDSPs sandwiched between a single seam plate, where the dimension of the FDSPs is shown in Fig. 1(c). And the overall structure is illustrated in Fig. 1(b). Other exhaustive values of the parameters are shown in Table 1. Because the proposed MS is symmetrical thus it possesses polarization insensitivity with the same response results in the transverse electric (TE) mode (where the electric field direction is along the +y-direction, magnetic field direction along the +x-direction and wave vector direction along the +z-direction) and the transverse magnetic (TM) mode (where the electric field direction is along the x-direction, magnetic field direction along the y-direction and wave vector direction along the z-direction). The simulation results were obtained through commercial simulation software High Frequency

Table 1 Detailed dimension

Parameter	a_1	a_2	a_3	d_1	d_2	d_3
Value (μm)	121	115.5	109	35	33.5	32
Parameter	l_1	l_2	l_3	w_1	w_2	w_3
Value (μm)	69.96	66.96	63.96	1.67	1.64	1.6
Parameter	t_1	t_2	t_3	h_1	h_2	n
Value (μm)	2.5	0.05	0.5	54.5	36	48
Parameter	w_4	l_4	u	k	h_3	h_4
Value (μm)	2.45	59.96	45	7	100	40

 This journal is © the Owner Societies 2023

Simulation Software (HFSS), in which the MS was arranged in a tight periodic alignment (similar to Fig. 1(a)). The incident wave is the plane wave on the structure with the boundary conditions being set as the periodic arrangement of elements in the $+x$ and $+y$ directions as well as the open boundary conditions in the $+z$ direction. The near-field coupling effects between adjacent unit cells were neglected but their effects have been considered and indicate that the formation principles are the same in the TE and the TM modes being vertically incident. As a result, the incidence in the TE mode is used as an example of the principle explained in the following discussion. Particularly, it is worth emphasizing that the incidence angle is considered as the angle in the *yoz* plane between the incident EM waves and the positive direction of the *z*-axis also defined as the angle in the *xoy* plane between the incident EM waves and the positive direction of the *x*-axis.

The proposed Janus MS is a multifunctional system that utilizes metal resonators to contribute to the PIT phenomenon when VO_2 functions as an insulator. As displayed in Fig. 3, the design process involved a gradual improvement from a one-layer to a three-layer structure, which resulted in the PIT effect being demonstrated in Fig. 4(a)–(c) across the different layer structures. The one-layer structure achieves a wide and high transparency window above 0.9 covering 2.079–2.270 THz. However, the unique structural design of VO_2 resulted in the formation of the anapole that localized a large amount of energy and created a high absorption point within the transparent window. The absorption $A(\omega)$ can be acquired by

$$A(\omega) = 1 - R(\omega) - T_z(\omega) - P(\omega) \quad (1)$$

where $R(\omega) = |S_{11}|_2$ represents reflectance, $T_z(\omega) = |S_{21}|_2$ indicates transmittance, and $P(\omega)$ denotes the conversion of polarization. As presented in Fig. 4(d)–(f), the peak point of forward absorption for the one layer structure was the highest, up to 93.90%. Nevertheless, the lowest point of the forward absorption on the right side was not as low as that of the three-layer structure. Regarding the backward absorption demonstrated in Fig. 4(g)–(i), the advantage of the three-layer structure is evident, forming a broadband absorption above 0.9 at 1.448–2.497 THz, which completely covers the transmission window generated by the metal resonators.

Based on our findings that the number of nested layers does not considerably affect the PIT and forward absorption, we concluded that our final design structure would be a nested three-layer structure as displayed in Fig. 1(a). When the metal structures acted alone, a transmission band above 0.9 between 2.052–2.220 THz was produced. When VO_2 was in a metallic state, the EM waves of 1.448–2.497 THz were reflected in the forward direction due to the cutoff frequency of the nested structure. Besides, as the EM waves are incident forward, the near-field interference between the anapole generated by VO_2 and the metal resonators results in energy absorption, creating the highest peak point at 2.154 THz in the reflection band. As the EM waves were incident backward, a broadband absorption between 1.448–2.497 THz was formed. The compound words "$-z$-direction" and "$+z$-direction" in Fig. 1(a) describe the wave vector *k*-direction. And we plan to further explore the multifunctional characteristics of the MS.

2.2 The mechanistic analysis of PIT behavior

In the design, the VO_2's conductivity is 10 S m^{-1} when the temperature is below 68 °C.[46] The FDSP acts as an insulator and has minimal effect on the other two metal resonators. Consequently, the two metal structures create a perfect broadband PIT. The transmission curves for the NR and CS responses in the TE mode are presented separately in Fig. 5(a) and 6(a), respectively. Additionally, electric field distribution diagrams for the two resonant frequency points in the TE mode and TM

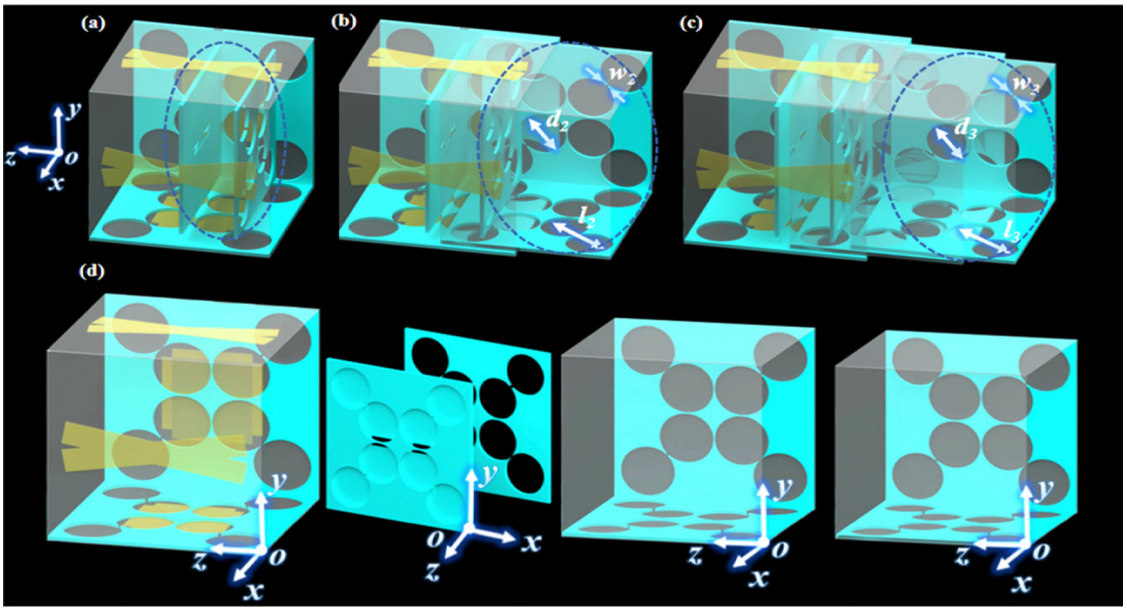

Fig. 3 (a) The one layer structure, (b) the two-layer structure, (c) the three-layer structure, and (d) a further clear representation of the circled structure.

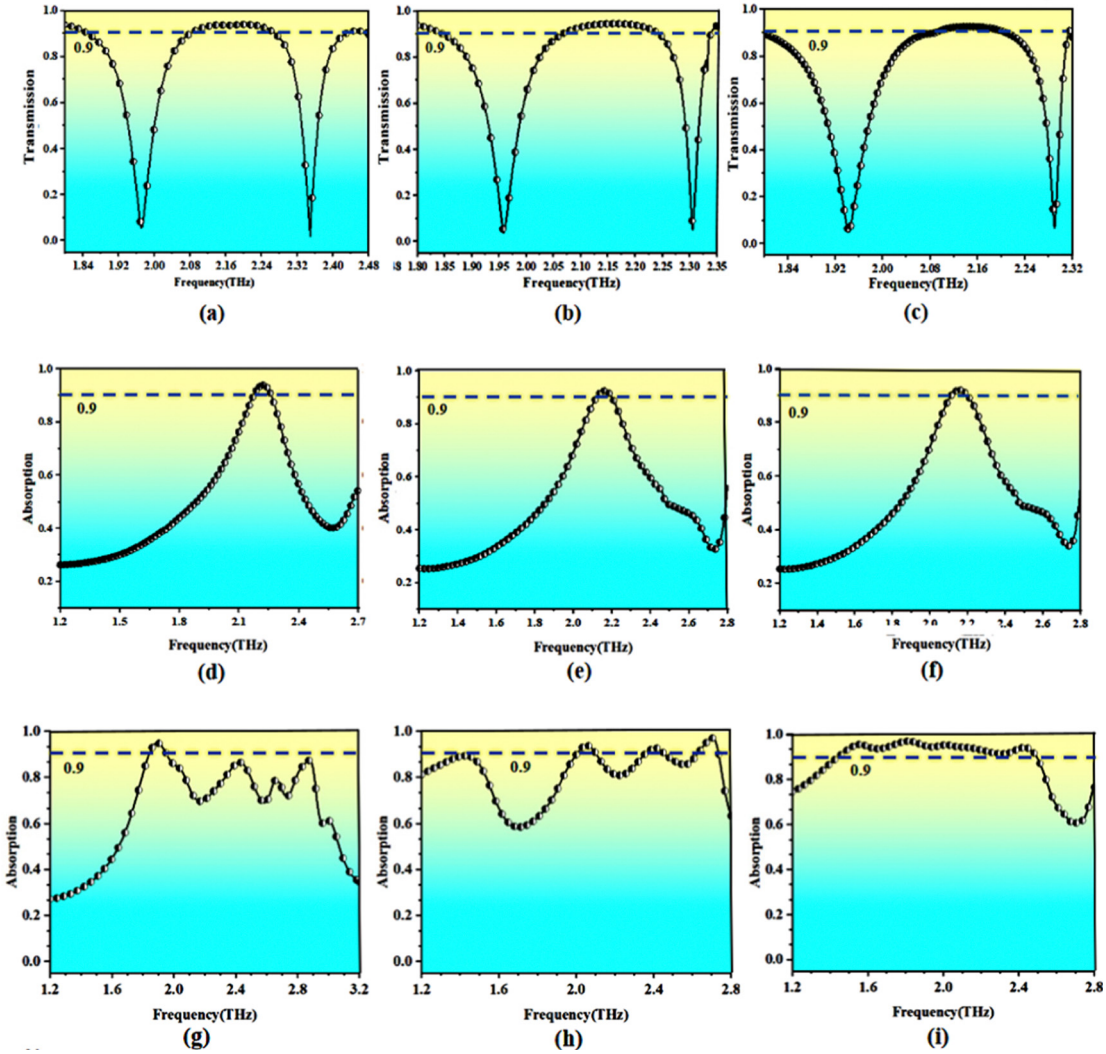

Fig. 4 Transmission curves of the PIT: (a) one layer formation with metal resonators, (b) two-layer formation with metal resonators, and (c) three-layer formation with metal resonators. Forward absorption curves: (d) one layer structure with metal resonators, (e) two-layer structure with metal resonators, and (f) three-layer structure with metal resonators. Backward absorption curves: (g) one layer structure with metal resonators, (h) two-layer structure with metal resonators, and (i) three-layer structure with metal resonators.

mode are provided in Fig. 5(b) and 6(b). From Fig. 5(b), it can be observed that the electric field concentrates at both ends, exhibiting a clear electric dipole characteristic in the same direction as the incident electric field. Furthermore, the cavity exhibits a lot of energy localities, as shown in Fig. 5(c). This observation proves that the resonance point results from the combination of electrical and cavity resonances. The NR can be excited directly by the incident EM waves at 1.906 THz, producing a bright mode resonance with a transmission dip of 0.023. A strong coupling between the NR and free space leads to a large radiation loss, resulting in a wide spectrum and a tiny Q value (quality factor $Q = f/\Delta f$, where f stands for the resonant frequency and Δf presents the half peak bandwidth) of 19.7 within the transmission spectrum.[47] In contrast, in Fig. 6(b), the transmission dip of 0.141 at 2.318 THz can be achieved by exciting the CS with the incident EM waves. The electric field energy remains gathered in the position parallel to the orientation of the incident electric field. However, as CS comprises two rectangles with a certain angle, it can only partially couple the electric field energy, leading to the generation of a quasi-dark mode electrical response. Fig. 6(c) also presents the effect of cavity resonance. Under the combined effect of both, the quasi-dark resonator gives birth to a large Q (483.2) resonance at 2.318 THz. In a word, the bright and quasi-dark mode resonators meet the requirements for PIT formation as the bright and dark modes have a large difference in Q values and similar resonant frequency points.

With the aim of demonstrating the coupling between bright and quasi-dark modes that cause the PIT phenomenon, we put the two resonators together for analysis. Specifically, the near-field coupling between NR and CS is examined, which gives rise to strong destructive interference. Bright and quasi-dark plasmon resonators exhibit individual resonance frequencies that are very close to the two resonant frequencies of the

 This journal is © the Owner Societies 2023

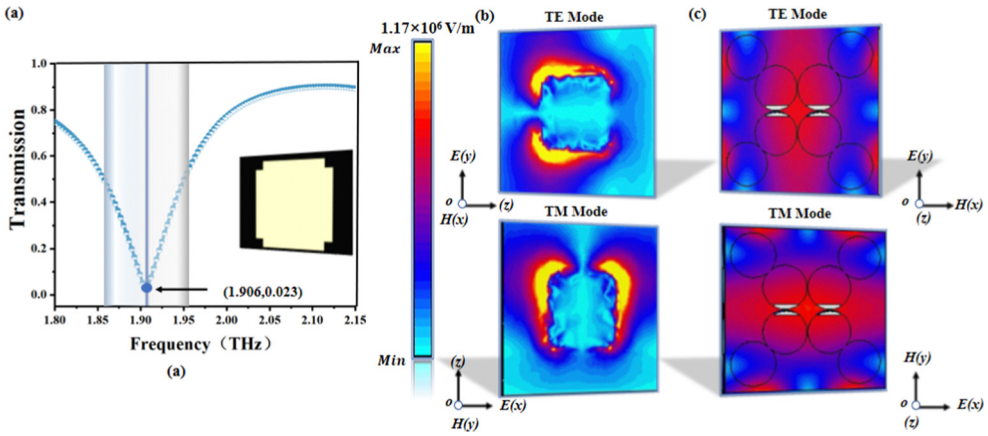

Fig. 5 The NR (bright plasmon resonator) resonates individually: (a) transmission response curve, (b) electric field distribution, and (c) electric field distribution in the cavity.

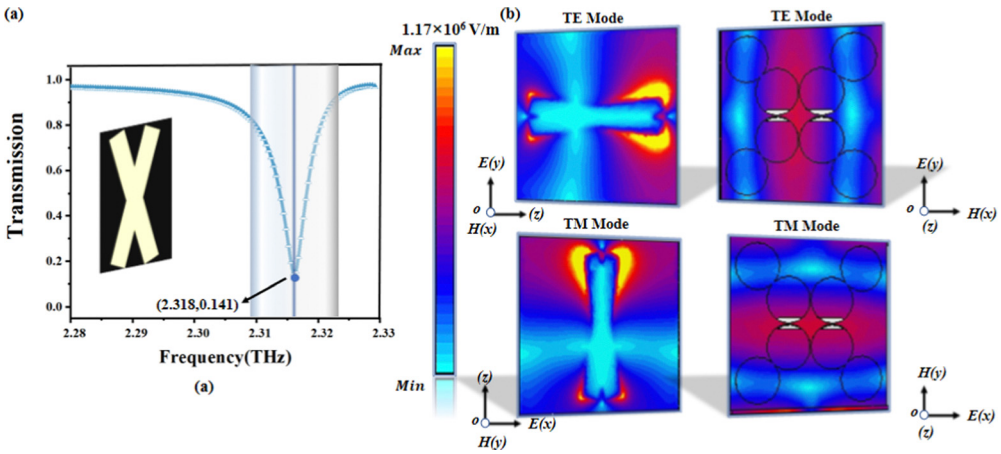

Fig. 6 The CS (quasi-dark plasmon resonator) resonates individually: (a) transmission response curve, (b) electric field distribution, and (c) electric field distribution in the cavity.

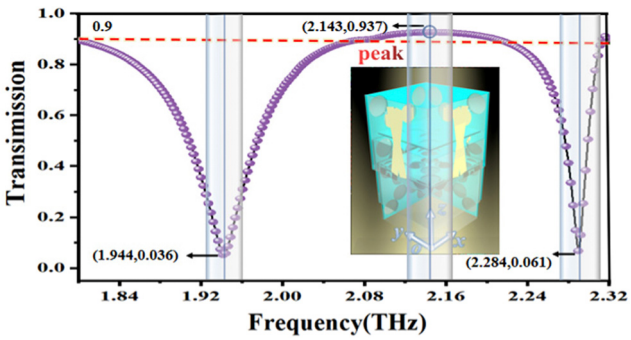

Fig. 7 The PIT transmission response curve.

complete PIT MS. Hence, a transmission window is generated from 2.052 THz to 2.220 THz as illustrated in Fig. 7. The transmission peak at 2.143 THz reaches up to 0.937.

To investigate the underlying mechanism, the surface current distribution charts at the transmission peak (2.143 THz) as well as two transmission valleys (1.944 and 2.284 THz) are plotted in Fig. 8 and 9. From Fig. 8(a), it is easy to observe that the surface current is concentrated at both ends of the axis parallel to the orientation of the incident electric field, indicating that the coupling with the incident EM waves cause the transmission point to drop at 1.944 THz. Analogously, it can be known from Fig. 8(b) that the transmission valley at 2.284 THz is created by an accumulation of electric fields on the CS, forming an energy locality. Furthermore, the surface current density at 2.143 THz, as depicted in Fig. 9(a), suggests that the near-field coupling between the localized plasmon resonance caused by the NR and the CS resonance leads to significant suppression of the initial excitation of the electric fields gathered on the two resonators owing to the incident field. In Fig. 9(b), the NR and the CS generate surface current in opposite directions and the radiation loss of the structure at 2.143 THz is enormously reduced, resulting in the appearance of the transmission peak. After generating destructive interference similar to that of classical three-level atomic systems, a wide transparent window covering 2.052 to 2.220 THz with a 7.4% relative bandwidth above 0.9 is achieved.

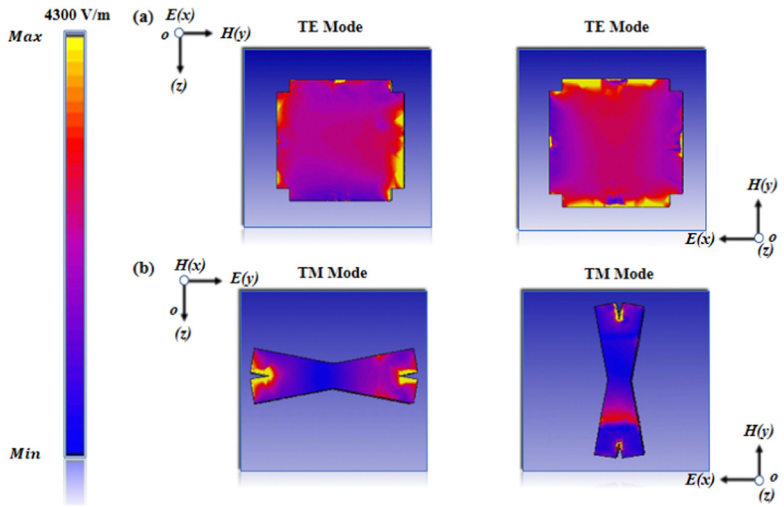

Fig. 8 The absolute value distributions of the surface current chart (a) at 1.944 THz, and (b) at 2.284 THz.

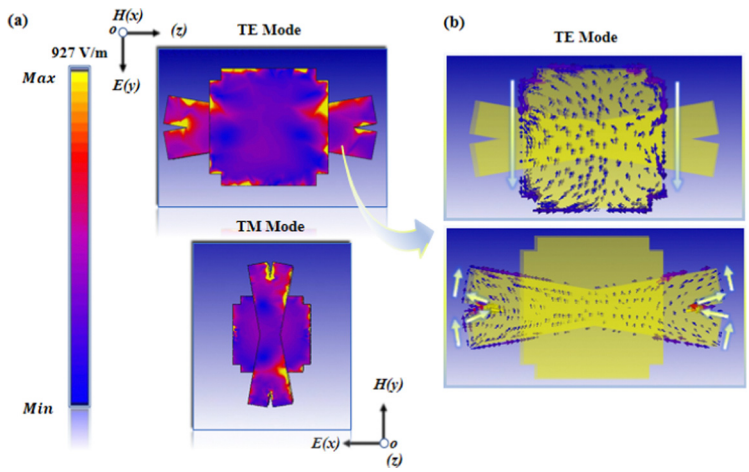

Fig. 9 (a) The absolute value distributions of surface current chart at 2.143 THz. (b) The surface current distributions chart at 2.143 THz.

The classic three-atom energy level theory is introduced with the aim of further explaining the generation of PIT. PIT is known as a quantum interference phenomenon, which results from the destructive interference of two laser fields with different frequencies on atoms in the absorption state. Specifically, this occurs when two distinct paths interfere with each other to produce the same atomic state. In Fig. 10, γ_1 and γ_2 represent the coupling coefficients between energy levels, and

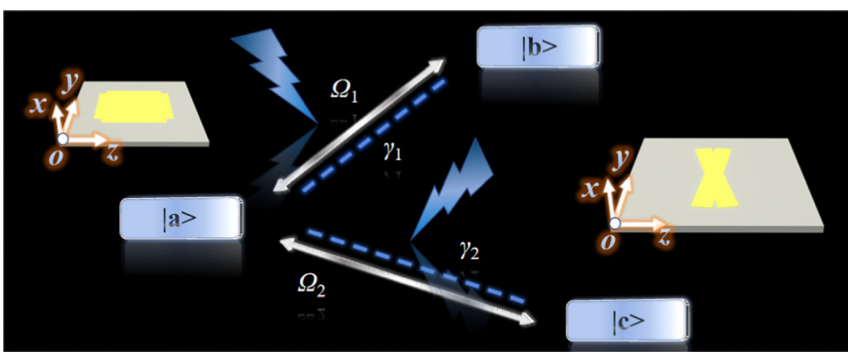

Fig. 10 The analogy between the classic three-atom system model and the PIT structure.

 This journal is © the Owner Societies 2023

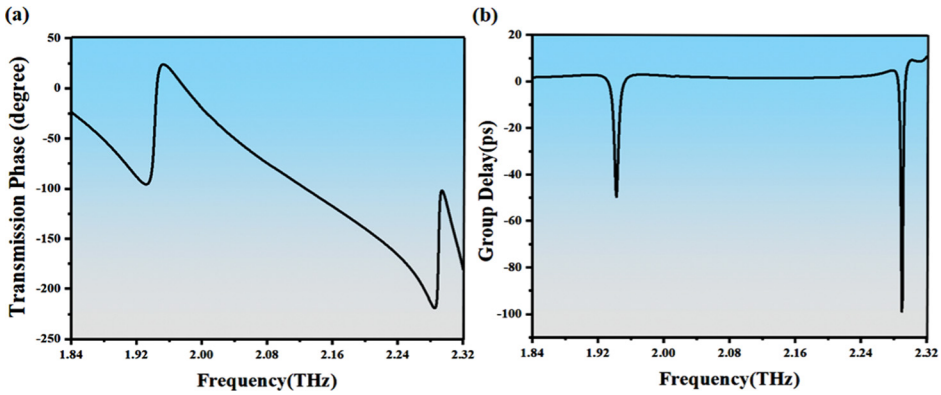

Fig. 11 Under the TE mode: (a) the transmission phase and (b) the GDs.

the phases of the two paths are donated by Ω_1 and Ω_2. When a weak coupling light is incident, the atoms in state $|b\rangle$ transition to state $|a\rangle$, and subsequently transition to a higher energy level $|c\rangle$ since $|a\rangle$ is unstable. In the presence of a much stronger incident probe light, the atoms in state $|c\rangle$ are excited and re-transition to state $|a\rangle$. Thus, two paths are generated on $|a\rangle$: $|b\rangle \rightarrow |a\rangle$ and $|b\rangle \rightarrow |a\rangle \rightarrow |c\rangle \rightarrow |a\rangle$. The two channels have almost equal and opposite amplitudes, resulting in a coherent cancellation on state $|a\rangle$.[48] This interference suppresses atom absorption, rendering the previously opaque medium transparent, visible as a transparent window in the broad absorption spectrum.

Based on the theory presented above, we can draw an analogy as the structure is equivalent to the three-atom energy level system shown in Fig. 10. That is to say, we can consider the unexcited NR and CS as $|b\rangle$ and $|c\rangle$ respectively. As the coupling light is present, the NR can be directly excited to the excited state, represented as $|a\rangle$. Following excitation, the NR will transfer energy to the CS. Although the CS can be directly excited by the incident field, the energy is insufficient to couple effectively with the NR. As the energy of the excited NR couples with the CS, the two energies are combined to generate a stronger wave, which is represented as the probing light. Subsequently, the energy of the CS can couple back to the NR, returning it to the $|a\rangle$ state. Consequently, two channels are formed: $|b\rangle \rightarrow |a\rangle$ and $|b\rangle \rightarrow |a\rangle \rightarrow |c\rangle \rightarrow |a\rangle$. Waves with almost equal amplitudes and opposite orientations are produced in the two channels, which create coherent interference and bring on the PIT phenomenon.

Simultaneously, a sudden phase transition of the transmitted signal within the transmission window attributes to a high group delay (GD), thereby giving rise to slow light effects and nonlinear interactions. The phenomenon of the slow light effect occurs when the group velocity (GV) of light in a vacuum is slower than the speed of light, which is due to dispersion. The calculation formula for GD can be expressed as eqn (2):[49]

$$\tau_{\mathrm{GD}} = -\frac{\partial \varphi}{\partial \omega} \tag{2}$$

in which φ, ω, c, and t denote the transmission phase, angular frequency, speed of light in a vacuum, and the total thickness of the design. Fig. 11(a) illustrates that two sudden phase jumps appear on the two sides of the PIT transmission window in the TE mode, which is consistent with the typical characteristics of PIT and facilitates the generation of slow wave propagation. Fig. 11(b) shows that the maximum of GD in the TE mode is 99 ps, providing a distinct slow light effect, which can be applied to various applications such as filtering, data storage, and optical slow waves.[50]

2.3 The physical mechanism of the anapole

At temperatures exceeding 68 °C, VO_2 undergoes a transition to a metallic state, which is characterized by a dramatic increase in its conductivity from 10 S m^{-1} to 3×10^5 S m^{-1}.[46] To generate an absorption point in the transmission window, FDSP composed of VO_2 on the side of the dielectric cavity (FDSPS) was designed to give birth to TP. In Fig. 12(a), the dumbbell-type aperture is distributed topologically along the diagonal. When the EM waves are incident vertically in the TE mode, the electric field can excite an oscillating charge perpendicular to the waist of the dumbbell aperture, inducing the generation of strong **P** pointing vertically in the diagonal direction, as described in Fig. 12(a). The oscillating charge produced by the incident EM waves forms two radial currents **J** flowing along the edge of the dumbbell aperture (marked with red arrows). In virtue of the presence of two reversed rotating currents **J**, two reversed MP moments **M** are produced. In Fig. 12(b), the **M** is connected at the beginning and end, generating **T** pointing diagonally perpendicular (marked with yellow arrows), while the **T** lags behind the **P** by a quarter (as displayed in eqn (3) and (4)).

$$\mathbf{P}(t) = \mathbf{P}e^{i\omega t} \sim (\pm x + y)\rho_0 e^{i\omega t} \tag{3}$$

$$\mathbf{T}(t) = \mathbf{T}e^{i\omega t} \sim (\pm x + y)i\omega\rho_0 e^{i\omega t} \tag{4}$$

The simulation results performed by the 3D EM simulation software HFSS reveal that the FDSPS is capable of producing a transmission curve that is comparable to that of the EIT depicted in Fig. 13(a). To investigate the mechanism of the FDSPS, Fig. 13(b) presents a summary of the numerical calculations consistent with the electric field strength. The scattering

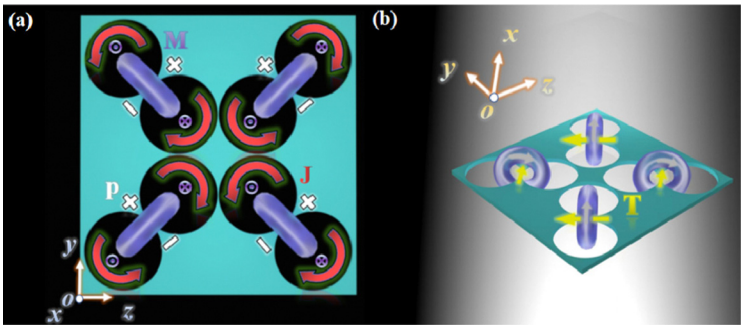

Fig. 12 (a) Schematic diagram showing the formation of **P**, **M** and **J**. (b) A chart showing the formation of **T**.

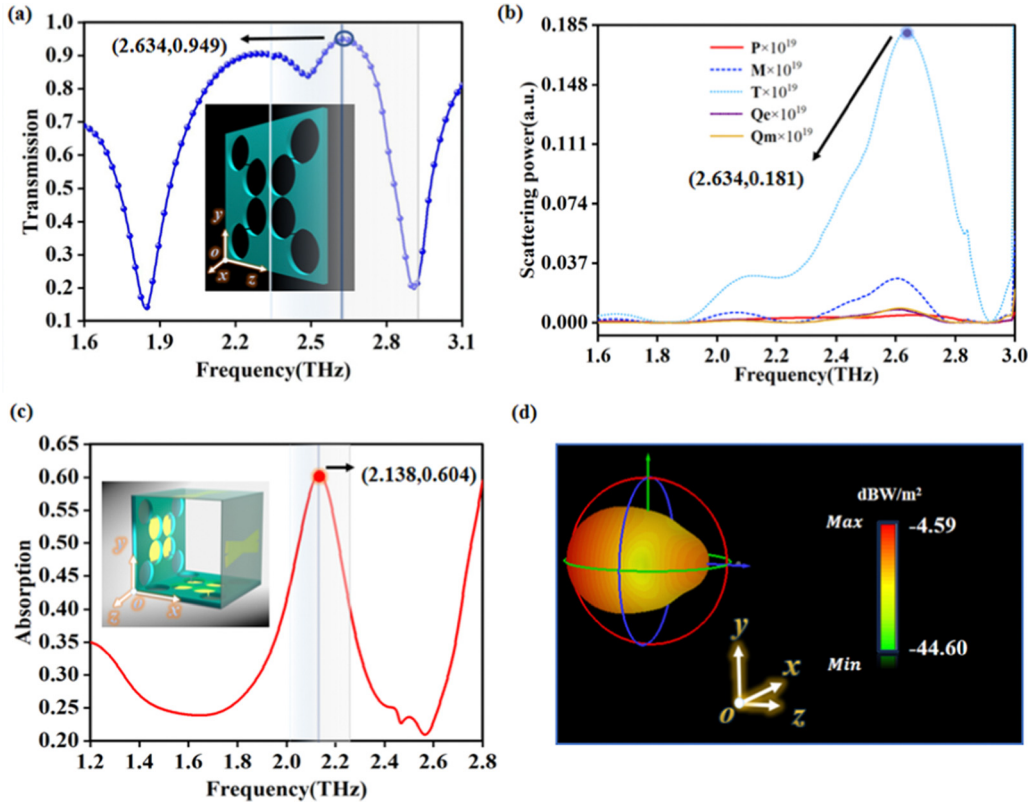

Fig. 13 (a) The transmission curve of the FDSPS. (b) The scattered powers by the incident radiation in the far zone. (c) The absorption curve when FDSPSs act with the NR and the CS. (d) The three-dimensional power radiation diagram of the FDSPM at f_A.

power of multipole moments is characterized by **P**, **M**, **T**, electric quadrupole moment $\mathbf{Q}_e$ and magnetic quadrupole moment $\mathbf{Q}_m$. By decomposing the scattering power, it is possible to reveal the relationship between the signature of multipole moment excitation in the near-field and the variation of electric and magnetic fields in the far zone. As evidenced by the results, the scattering power of the TP attains its maximum at 2.634 THz, which corresponds to the peak of its transmission curve. Notably, the scattering power of the TP is significantly higher than that of other multipoles, and it reaches a maximum of 0.604 at 2.138 THz when the FDSPS interacts with the metal resonators, indicating that the formation of the EIT is a consequence of the action of the TP. And the plot in Fig. 13(c) suggests that an absorption point with an absorptivity of 0.604 is formed at 2.138 THz when FDSPSs act with the NR and the CS, causing interference and energy absorption in the near field.

For the sake of further enhancing the absorption peak, we placed the FDSP in the direction perpendicular to the z-axis, denoted as FDSPM, where the vector sum of **P** present in the FDSPM points in the y-direction. Likewise, the vector sum of **T** present in the four apertures also points in the y-direction. Because the EP and the TP always maintain a phase difference of 90°, thus the phase difference between the two radiated electric fields can reach 180°. The radiation electric field $E_{\mathbf{P}(t)}$

 This journal is © the Owner Societies 2023

generated by **P** is manifested in eqn (5), while the radiation electric field $E_{\mathbf{T}(t)}$ excited by **T** is described by eqn (6),[51]

$$\mathbf{E_P} = \left[\frac{F(\omega,r)(\mathbf{r}\cdot\mathrm{P})}{c^2r^2}\mathbf{r} - \frac{G(\omega,r)}{c^2}\mathrm{P}\right]\frac{\exp(-\mathrm{i}kr+\mathrm{i}\omega t)}{r} \tag{5}$$

$$\mathbf{E_T} = \left[\frac{\mathrm{i}kG(\omega,r)}{c^2}\mathbf{T} - \frac{\mathrm{i}kF(\omega,r)(\mathbf{r}\cdot\mathrm{T})}{c^2r^2}\mathrm{P}\right]\frac{\exp(-\mathrm{i}kr+\mathrm{i}\omega t)}{r} \tag{6}$$

where k, c, and r, represent the wave vector, speed of light in vacuum, and the coordinate vector, respectively. As the wavelength of the incident EM wave is close to the circumference of the elliptical toroidal structure, the radiation intensity of **T** is gradually improved. Since its radiation intensity is close to **P**, the excitation of the anapole mode is formed, giving birth to destructive interference. The description is given for the condition that ensures destructive interference in eqn (7),[51]

$$\mathbf{P} = \mathrm{i}k\mathbf{T} \tag{7}$$

The equation presenting **T** is shown as follows:[51]

$$\mathbf{T} = \frac{1}{10c}\int \mathrm{d}^3r\left[\mathbf{r}(\mathbf{r}\cdot\mathrm{J}) - 2\mathrm{J}r^2\right] \tag{8}$$

while **P** can be described by eqn (9),[51]

$$\mathbf{P} = \frac{1}{\mathrm{i}\omega}\int \mathrm{d}^3r\mathrm{J} \tag{9}$$

Under the assumption that **T** and **P** are located at the origin (r = 0), the radiated electric field $\mathbf{E}_{\mathrm{total}}$ and the magnetic field $\mathbf{H}_{\mathrm{total}}$ produced by the superposition of two dipoles are given by the following equations,[51]

$$\begin{aligned}\mathbf{E}_{\mathrm{total}} &= \mathbf{E_P} + \mathbf{E_T}\\ &= \left[\frac{(\mathbf{r}\cdot\mathrm{P}-\mathrm{i}k\mathrm{T})F(\omega,r)}{c^2r^2}\mathbf{r} - \frac{G(\omega,r)}{c^2r}(\mathrm{P}-\mathrm{i}k\mathrm{T})\right]\\ &\quad\times\frac{\exp(-\mathrm{i}kr+\mathrm{i}\omega t)}{r}\end{aligned} \tag{10}$$

$$\begin{aligned}\mathbf{H}_{\mathrm{total}} &= \mathbf{H_P} + \mathbf{H_T}\\ &= -\frac{\mathrm{i}kD(\omega,r)}{cr}[\mathbf{r}\times(\mathbf{P}-\mathrm{i}k\mathbf{T})]\frac{\exp(-\mathrm{i}kr+\mathrm{i}\omega t)}{r}\end{aligned} \tag{11}$$

We can conclude that the anapole response occurs when **P** = ik**T** by eqn (10) and (11), with superimposed electric and magnetic fields vanishing at the far field. At the near field (r = 0), its EM energy is localized in large amounts. Eqn (12) and (13) indicate that the electric field is concentrated at a specific point in the near field when anapole resonance is produced, and the magnetic field is distributed in a loop perpendicular to the electric field direction.

$$\mathbf{E}_{\mathrm{total}}\ (r=0) = \mathrm{i}k\mathbf{T}\delta(\mathbf{r})\exp(\mathrm{i}\omega t) \tag{12}$$

$$\mathbf{H}_{\mathrm{total}}\ (r=0) = \mathrm{i}k\mathrm{rot}[\mathbf{T}\delta(\mathbf{r})]\exp(\mathrm{i}\omega t) \tag{13}$$

Further validation is required to confirm the features of the anapole mode in the FDSPM. The power scattered by multipole moments including **P**, **M**, **T**, $\mathbf{Q}_{\mathrm{e}}$, and $\mathbf{Q}_{\mathrm{m}}$, and the numerical calculations in accordance with current density are summarized in Fig. 14(a). What can be deduced is that the scattering power of **P** and **T** is much larger than that of the other multipoles around f_{A} = 2.06 THz, proving that **P** and **T** play a dominant role in the scattering process. In the engineered configuration, the scattering power of dipole moments other than **P** and **T** are suppressed, resulting in weak responses in the spectrum at f_{A}. Interestingly, the **P** and **T** exhibit equal amplitude of scattering power and their corresponding phases shown in Fig. 14(b) achieve zero at f_{A}. Therefore, an anapole mode emerges at f_{A}, inducing strong field enhancement and destructive interference. The anapole mode is a typical Fano resonance, which will produce the asymmetric EIT phenomenon plotted in Fig. 14(c).[51] In the TE mode, this single-layer FDSPM can obtain a maximum transmittance of 0.764 at f_{A}. The position of the transmission peak coincides with the anapole resonant frequency, which further confirms the previous theoretical analysis. For the sake of further demonstrating this phenomenon, we observed the three-dimensional power radiation diagram of the FDSPM at f_{A} in Fig. 13(d). It is obvious that the presence of FDSPM greatly suppresses the power radiation in the far field, and the maximum difference of the power maps reaches −4.585 dBW m^{-2}, which fully proves the proposed absorption enhancement strategy is well demonstrated.

To further substantiate the near-field properties of the single-layer DPSM, EM simulations to visualize the distributions of the electric and magnetic field at the anapole resonant frequency f_{A} are conducted, and the outcomes are depicted in Fig. 15. Specifically, in Fig. 15(a), we observed that the incident EM waves trigger the generation of numerous currents distributed along the edge of the dumbbell-shaped aperture, which is consistent with the prior theoretical analysis. Additionally, from Fig. 15(b), it can be deduced that a vertical incident wave with the frequency of f_{A} leads to the formation of multiple vector rings with connected heads and tails in the magnetic field vectors located around the FDSPM cell structure, thus indicating the presence of the **T**. Apart from that, the magnetic field distribution correlates well with the electric field distribution demonstrated in Fig. 15(a), which provides additional support for the previous statements regarding the electric field distribution. In summary, the distributions of the induced vector current and vector magnetic field provide further evidence of the anapole formation mechanism.

In contrast, the comparison reveals that the absorption peak is more pronounced when the FDSPM of the double-layer structure (FDSPMs) displayed in Fig. 14(d) operates independently, bringing about an absorption peak above 0.8 at 1.895 THz in Fig. 16(a), which can be explained as the FDSPMs induce a decrease in the value of the prior transmission window to 0.444, thus improving the absorptivity.

To further develop the structure with different front and back absorption features, a single slit structure made of VO_2 is added behind the first FDSPM layer just like what is plotted in Fig. 14(e). Controlling the unidirectional no-reflection phenomenon can be implemented by regulating the coupling between the FDSPMs and the single-slit plate. As described in

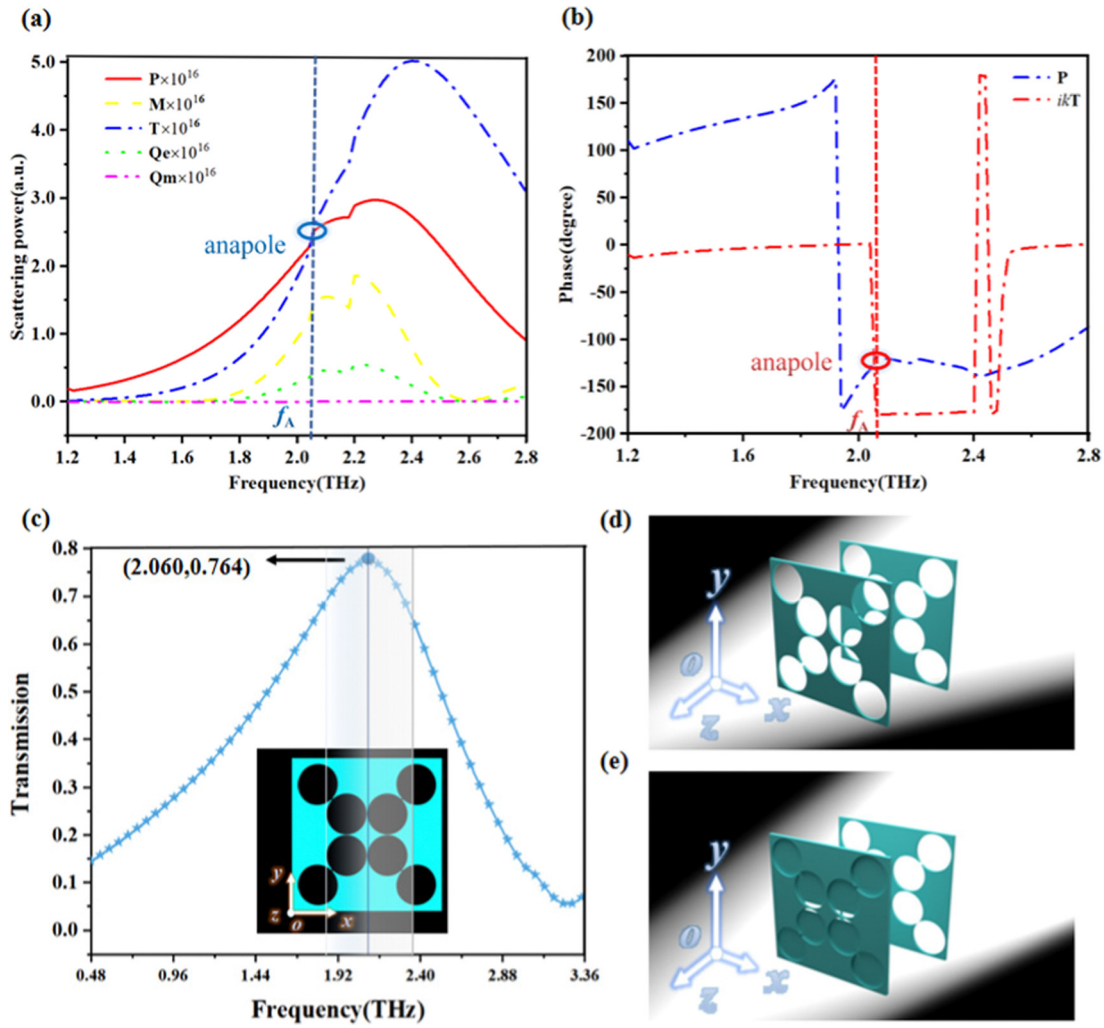

Fig. 14 (a) The scattered powers of **P**, **M**, **T**, $\mathbf{Q}_e$ and $\mathbf{Q}_m$. (b) Phases of **P** and i*k***T**. (c) The transmission curve of the FDSPM. (d) Schematic of the double-layer FDSPMs. (e) Schematic of the double-layer FDSPMs sandwiched with a single slit structure made of VO_2.

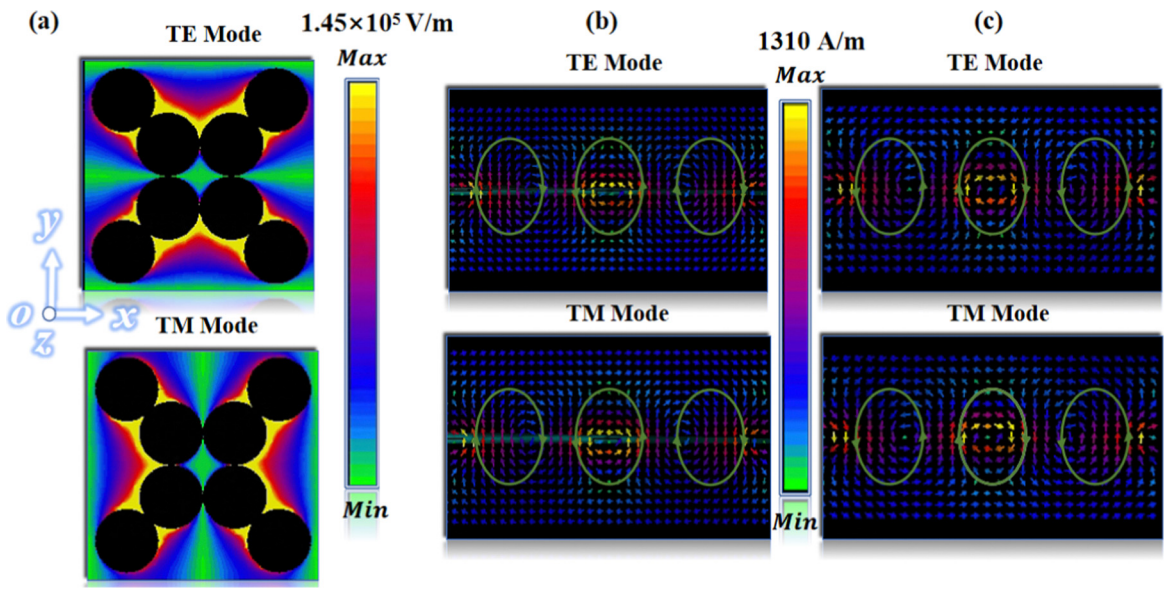

Fig. 15 (a) The absolute value distribution of the surface current chart. The magnetic field distribution at perpendicular incidence in the TE mode: (b) cross section along the diagonal $y = -x$; (c) cross section along the diagonal $y = x$.

 This journal is © the Owner Societies 2023

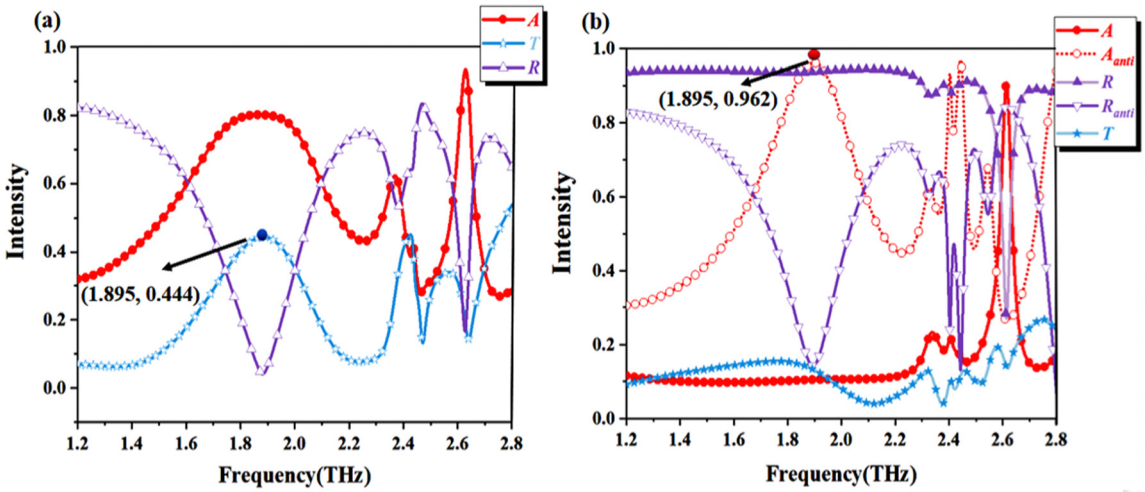

Fig. 16 (a) The EM properties of the double-layer FDSPMs in the TE mode, in which A represents absorption, T_z donates transmission, and R presents reflection. (b) The EM properties of the double-layer FDSPMs united with the single silt plate, in which A represents the forward absorption, A_{anti} represents the backward absorption, T_z donates the forward transmission, $T_{z(anti)}$ donates the backward transmission, R presents the forward reflection and R_{anti} presents the backward reflection.

Fig. 16(b), when they interplay together, an anomaly emerges in the backward reflection at 1.895 THz, making the backward absorption approach 0.962, while the forward absorption is all approximately 0.1 within the range of 1.2–2.2 THz with a single peak absorption point of 0.908 at 2.614 THz. Nevertheless, while they interact together with the previous structure, the backward absorption performance is less advantageous than expected, as we can see in Fig. 4(g). In a bid to further bettering the discrepancy between the forward and backward absorption, uniting two more layers of FDSPs nested structures in the +z-axis direction is mandatory.

2.4 The physical mechanism of the SSPPs

The size of the FDSPSs placed on the internal dielectric cavity decreases in the −z-direction, so when the EM waves are incident forward and reverse, the corresponding cutoff frequency is also inconsistent. The largest and the smallest FDSPS are equipped with the cut-off frequency of f_{min} and f_{max}.[52] When the EM waves are incident (propagating in the −z-direction), transmission at $f > f_{max}$ as well as scattering in $f_{min} < f < f_{max}$ will develop in the FDSPSs. Otherwise, when f is equal to f_A, the anapole resonance is generated, creating a high absorption point in the reflection band. However, the characteristics of this MS change dramatically when the EM waves propagate in the +z-direction. In the case where the frequency f exceeds the f_{max}, direct transmission through the structure is possible. However, when the frequency f falls within the range of f_{min} to f_{max}, the waves are coupled to the surface of the structure, leading to broadband absorption.

To verify the mechanism of the frequency selective absorption in FDSPSs, the auxiliary plane A in Fig. 17(a) is introduced, and the electric field distribution on the FDSPSs at plane A is shown in Fig. 17(b)–(e). The electric field is observed to be stronger on specific FDSPS in the absorption segment, with the effects moving towards the +z-direction when the frequency of the incident wave increases. At 1.8 THz, 2.2 THz, 2.4 THz and 2.7 THz, the electric field mainly concentrates on the interface between FDSPSs and the substrate, guided by the SSPPs. As the frequency of the incident EM waves climbs, the electric field gradually shifts from the top FDSPS to the middle and then to the bottom of the array, indicating that EM waves resonate on specific FDSPS at certain frequencies, enhancing the electric field. In contrast, there is a faint electric field effect at 2.7 THz, as shown in Fig. 17(e), suggesting the possibility of transmission. The phenomena prove that SSPPs can be generated effectively and have desirable characteristics at different stages.

The effect of the forward and backward absorption of the MS is well manifested in Fig. 18(a). Furthermore, Fig. 18(b) exhibits the frequency-dependent variation in R, R_{anti}, T_z, and $T_{z(anti)}$ when a vertically EM wave in the TE mode is incident in positive and negative directions. Notably, when the wave in the TE mode is vertical incident forward, the MS achieves an absorptivity of 0.921 around 2.154 THz thanks to the TPs and EPs. However at other frequencies, the majority of the forward incident EM waves can be reflected. As the wave is reversely and vertically incident in the TE mode, the MS develops an absorption above 0.9 in the band of 1.448–2.497 THz. Besides, the reversely incident EM waves can be reflected at 2.707 THz with a reflectivity reaching 0.386. The simulation-based EM characteristics of the MS are consistent with the theoretical analysis presented above.

To gain insights into the working behavior of the MS in response to EM waves propagating in the −z and +z directions, it is essential to investigate the EM waves flowing in the structure. Thus we introduced auxiliary planes A, B and C, as shown in Fig. 17(a), to monitor the power flow more explicitly. Fig. 19 displays the energy flow results at characteristic frequencies of 1.4 THz and 2.154 THz, which can provide further insights. The results at plane A prove that for an incident wave frequency of 1.4 THz, the majority of EM waves are reflected by

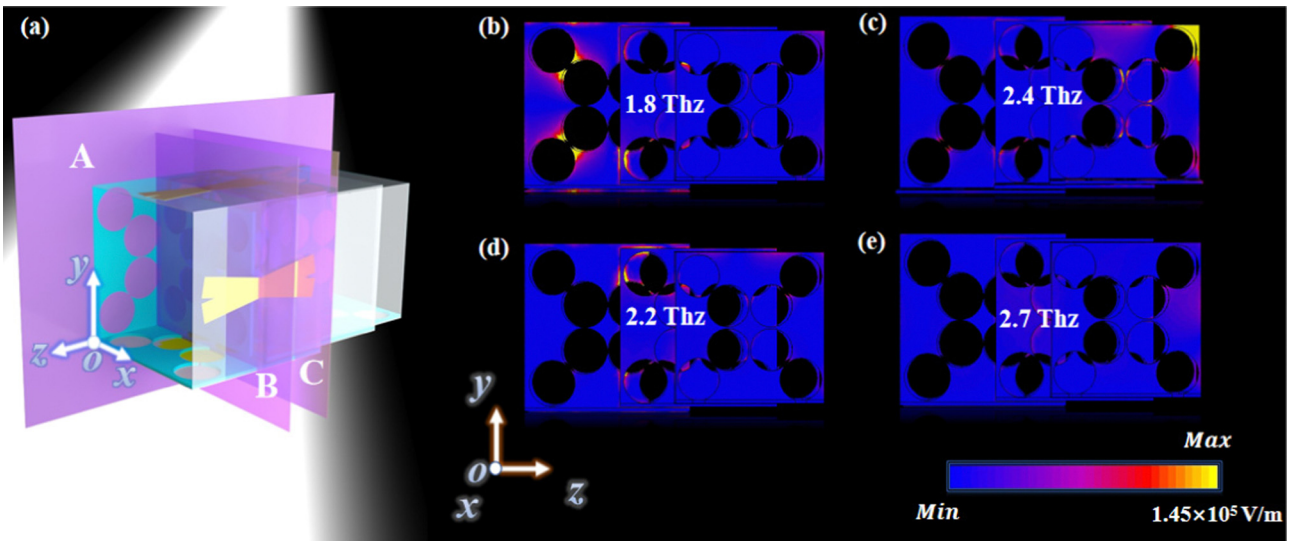

Fig. 17 (a) A schematic representation of auxiliary planes A, B, and C. The electric field at specific frequencies on the FDSPS in the +z-direction: (b) at 1.8 THz, (c) at 2.2 THz, (d) at 2.4 THz, and (e) at 2.7 THz.

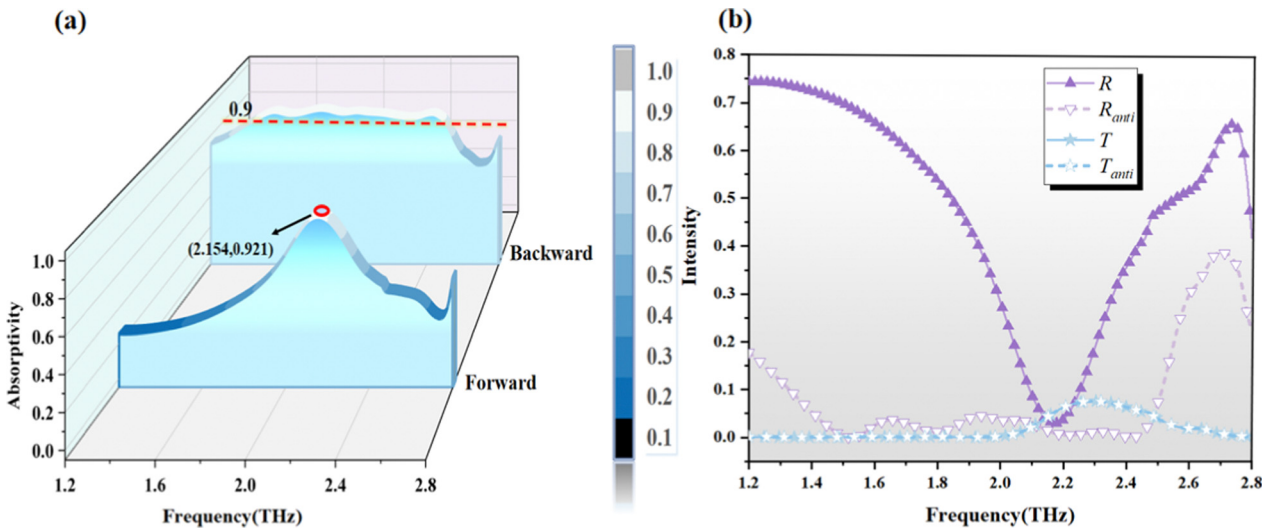

Fig. 18 (a) The forward and the backward absorption of the MS. (b) The intensity of R, R_{anti}, T_z and $T_{z(anti)}$ of the structure.

the first layer FDSPM and the single slit in the −z-direction. Fig. 19(a) clearly depicts that only a small portion of the EM waves are able to pass through. When it comes to the incident wave propagating in the +z-direction at 1.4 THz in Fig. 19(c), most of the energy is localized in the nested structure of FDSPSs, and there are barely EM waves to pass through, resulting in the high backward absorption. We also analyze the energy flow at the highest point of the forward absorption. As shown in Fig. 19(b), when the EM waves are incident along the −z-direction, annular energy flows are formed near the nested FDSPSs at plane B and plane C, indicating that the energy localization of the TPs prevents the propagation of energy and greatly reduces the transmittance. Combined with the energy flow analysis of the FDSPMs and the simple slit as plotted in Fig. 19(e), we can also find that the energy is localized in the dumbbell-shaped structures of the FDSPMs. As the EM waves propagate along the +z-direction shown in Fig. 19(d), it could be seen that circular energy flows are also developed near the FDSPSs, and the FDSPMs in the middle layer play a brilliant role in energy blocking.

2.5 Parameter discussion

Intending to preferably explore the impact of parameters on the performance of the MS and consider the coupling distance between nested structures, Fig. 20 presents a key parameter that is believed to have an essential effect on the absorption, namely h_2, which represents the distance between the second-layer FDSPM and the first-layer FDSPM and is known to significantly affect the absorption due to its role in adjusting the coupled phase between them.[53] In Fig. 20(a), the results are

 This journal is © the Owner Societies 2023

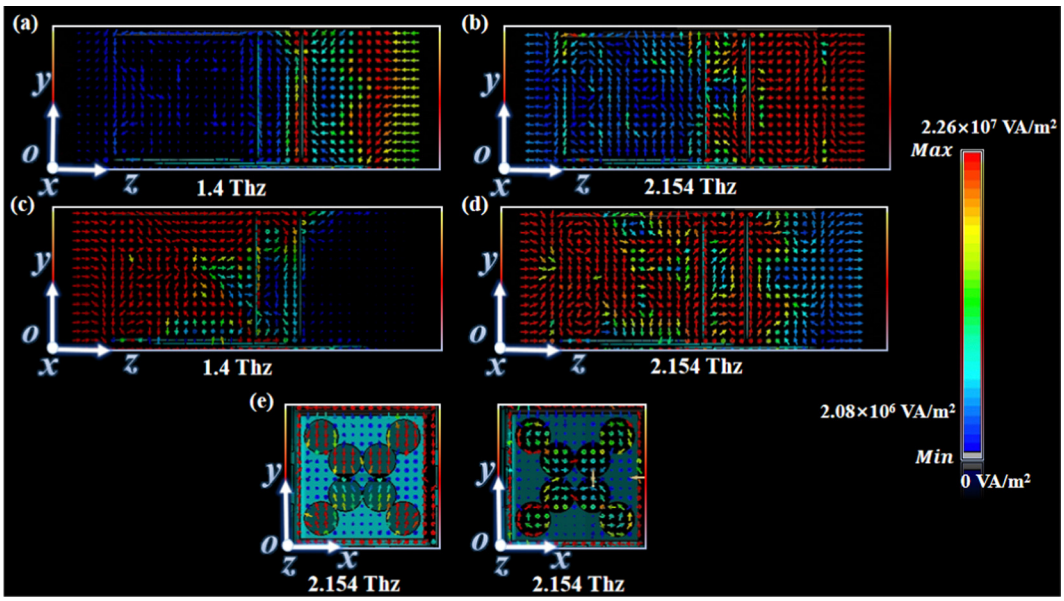

Fig. 19 The power flow normalized results at the auxiliary plane A perpendicular to the x axis under the $-z$-direction passing the MS: (a) at 1.4 THz and (b) at 2.154 THz. The power flow normalized results at the auxiliary plane perpendicular to the x axis under the $+z$-direction passing the MS: (c) at 1.4 THz and (d) at 2.154 THz. The power flow normalized results at the auxiliary plane B and C perpendicular to the z axis under $-z$-direction passing the MS: (e) at 2.154 THz.

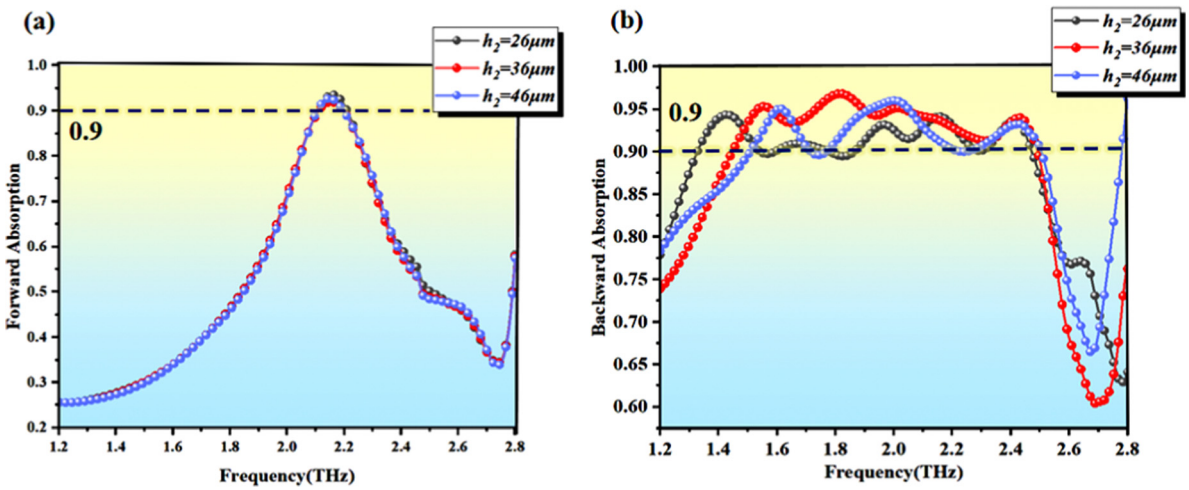

Fig. 20 (a) The forward absorption of the MS in the TE mode as h_2 varies. (b) The backward absorption of the MS in the TE mode as h_2 varies.

almost identical for the forward absorption, while substantial differences are provided in the absorption curves for the backward absorption at varying h_2 values. As depicted in Fig. 20(b), increasing h_2 causes a redshift in the backward absorption as the frequency varies from 1.322–2.462 THz to 1.498–2.507 THz. Moreover, at h_2 values of 26 μm and 46 μm, the absorption in some frequency bands has already fallen below 0.9, with the highest absorption peak values being 0.944 and 0.960, respectively, both of which are lower than the final proposed structure's absorption peak value of 0.969. We can understand in this way, the absorption point of the forward absorption is mainly formed by the action of TPs and EPs, and the change of h_2 only adjusts the coupling between nested structures and does not affect the anapole mode. Thus, as h_2 changes, the effect on the forward absorption is negligible, while the effect on the backward absorption is relatively large.

Except for the above parameter, we also discuss the impact of the incident angle of the incident waves on the MS. Fig. 21 presents the curves of the forward and backward absorption of the MS under different incident angles in the TE and TM modes. From Fig. 21(a), the forward absorption peak value increases initially as the incident angle changes from 0°, and then decreases with higher absorption developed on both sides. It can be observed that when the incident angle is 80°, the absorption value at the original absorption peak position is around 0.1. What is also worth noticing is that a low absorption

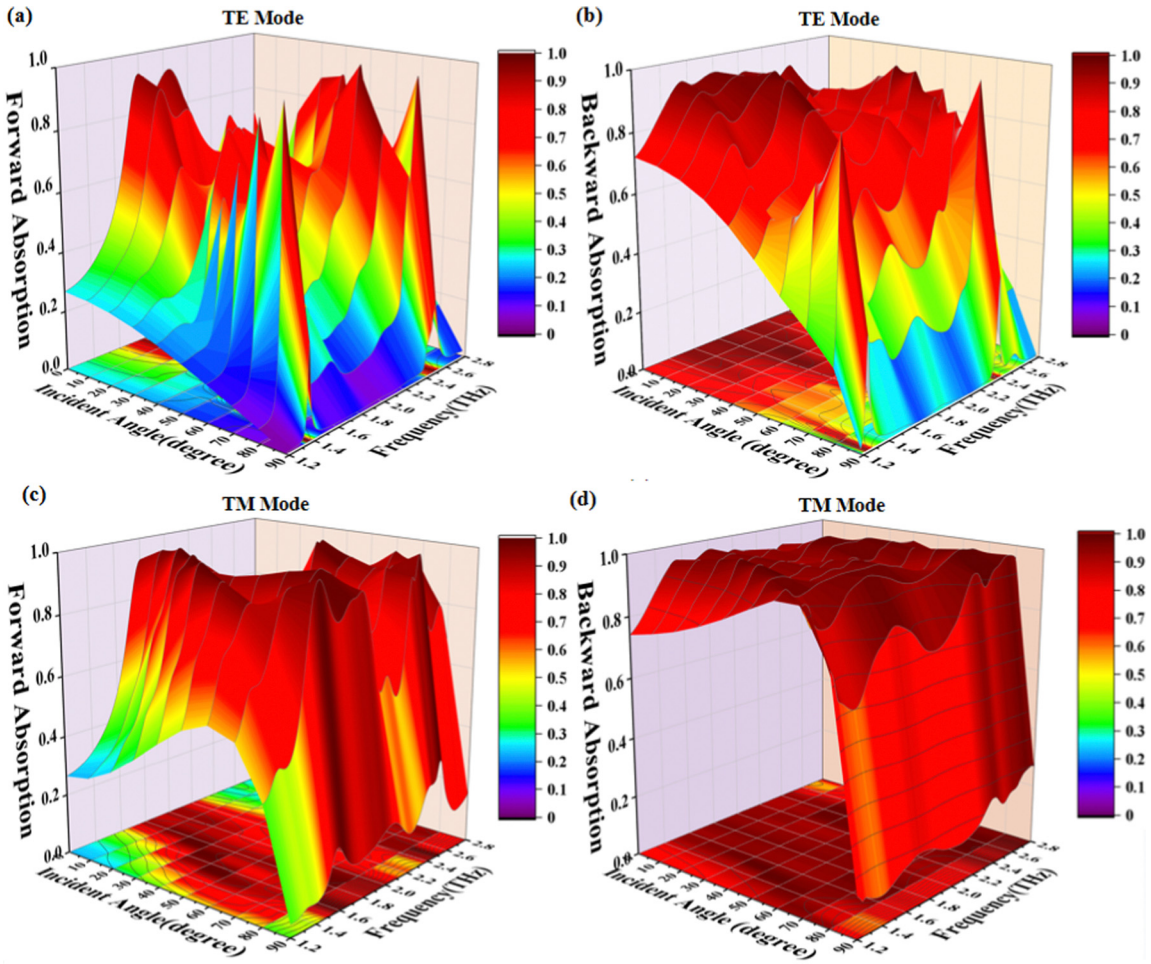

Fig. 21 The absorption at different incident angles (varying from 0° to 90°): (a) the forward absorption for the TE mode, (c) the forward absorption for the TM mode, (b) the backward absorption for the TE mode, (d) the backward absorption for the TM mode.

a band below 0.1 between 1.552–2.110 THz comes into being. Furthermore, two absorption peak points are formed at 1.383 THz and 2.492 THz on both sides of the low absorption band, with absorptivity of 0.990 and 0.892, respectively. While the incident angle continues to increase and approaches 90°, both absorption peak values decrease dramatically, arousing the consequence that the EM waves are almost completely reflected. This reveals that the MS exhibits remarkable angle sensitivity, and its absorption performance can be adjusted by modifying the incident angle, thereby converting the absorption band into a complete reflection band and providing two variable absorption points with excellent absorption performance. With respect to the backward absorption in the TM mode elucidated in Fig. 21(b), the overall absorption performance shows a decreasing trend with an increase of the incident angle. When it boosts to 40°, a wideband absorption above 0.6 from 1.2 to 2.8 THz emerges. With the further raise of the incident angle, a similar effect as the forward absorption appears, that is to say, absorption peaks are formed on both sides of the low absorption band at 1.257 THz and 2.404 THz with absorption values of 0.943 and 0.993, respectively. This phenomenon in this work is influenced by the incident angle, which affects the arrival time of the electric field component of the EM waves on the diverse resonant structures. As a result, there are variations in the modulation effect. These angle characteristics have promising applications in the field of detection.

In view of the forward absorption, as the incident angle varies gradually from 0° to 10°, the absorption peak increases from 0.921 to 0.960 in the TM mode in Fig. 21(c). Beyond this range, particularly between 30°–70°, the broadband high absorption is formed. As the incident angle approaches 90°, the previous absorption peak is 0.330, primarily below 0.2. This effect is even more pronounced by observing the backward absorption in Fig. 21(d). As the incident angle changes from 0°–70°, the absorption above 0.9 is achieved within 1.2–2.8 THz, while at incident angles close to 90°, total reflection is developed. This change is attributed to that in the TM mode, plasma resonance occurs at specific incident angles, resulting in energy localization and donating a super-broadband absorption. To explore the absorption impact of the TM mode, we expanded the frequency range to 0.1–10 THz and found distinctive absorption effects. Within the range of 0.7–10 THz, an ultra-wide absorption band with the absorption value of almost all

 This journal is © the Owner Societies 2023

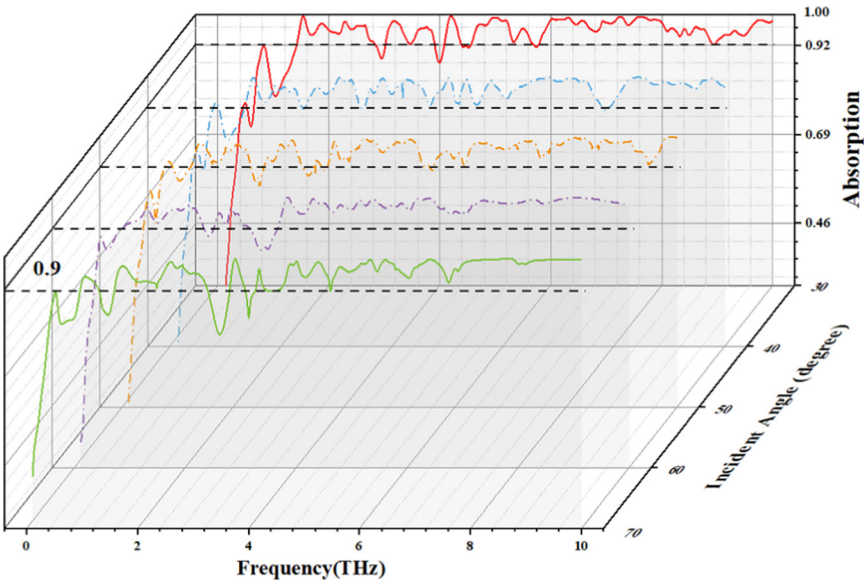

Fig. 22 Absorption variation curves for the incidence angle varying from 30° to 70° in the TM mode (in the +z-direction).

above 0.9 is formed as the incident angle varies from 30°–70° in the +z-direction in Fig. 22. We can understand it in this way, in the TM mode, when the incident angle rises, the electric field component for the FDSPSs is greater than the loss of the intermediate FDSPMs by the magnetic field, so the absorption increases instead of dropping.

The polarization properties of the structure are also scrutinized in this study. The MS's symmetry contributes to its predictable polarization insensitivity. Fig. 23(a) reveals that the two absorption lines above 0.9 for the forward absorption are essentially circular, manifesting that the absorption peak and bandwidth are minimally affected by the change in polarization angle. As shown by the backward absorption presented in Fig. 23(b), the influence on the absorption at higher frequencies is negligible, while the absorption at 1.52–1.83 THz fluctuates around 0.9. As a whole, our structure demonstrates polarization insensitivity, and the MS presents novel ideas for the future design of high-quality polarization-insensitive MSs.

After a meticulous review of the recently published relevant studies, which demonstrate tunable characteristics,[54–57] it has come to our attention that the prime merit of the structure we devised lies in its ability to manifest remarkable Janus properties. Notably, compared to the proposal designed by Mou *et al.*,[58] our MS exhibits an unparalleled wideband absorption capacity ranging across 0.7 to 10 THz when confronted with backward incident EM waves, showing excellent incident angle stability. This prominent feature sets our design apart from other existing alternatives. To highlight the unique features of Janus MS, specific parameters related to multitasking from previous research are presented in Table 2. These parameters

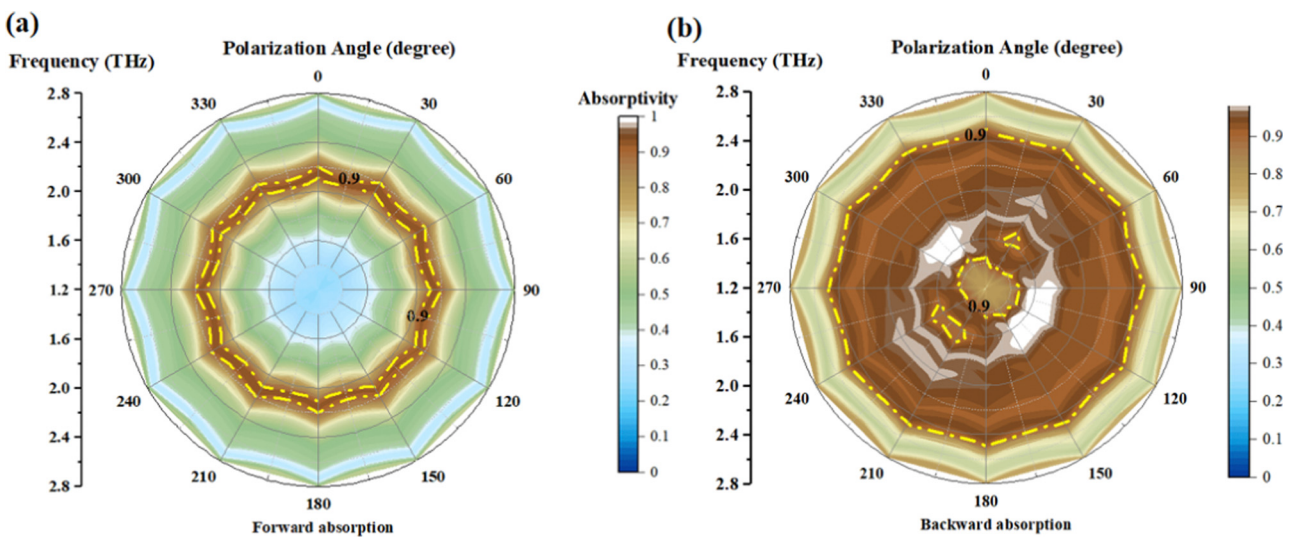

Fig. 23 The absorption at different polarization angles (changing from 0° to 360°): (a) the forward absorption, and (b) the backward absorption.

Table 2 A comparative evaluation of different works

Research	Tunable material	Variables	Adjustment section	Functionality	Optimum performance parameters	Ultrawideband absorption or not
Ref. 59	Insb	Temperature	Working band	Absorber	0.4–2.2 THz	No
Ref. 60	Graphene, VO_2	Voltage, temperature	① Functionality ② Efficiency	① Absorber ② Reflection	① 46–54 THz	Yes
Ref. 61	None	Direction of the incident wave	Functionality	① Anomalous refraction ② One-way focusing ③ Asymmetric focusing	The cross-transmission amplitude >0.7	No
Ref. 62	None	Polarization state of the incident waves	The place of focal segments	Light sword lens	—	No
Ref. 63	None	Direction of the incident wave	Transmission or reflection	① Two reflection channels ② Two transmission channels	The coefficients of the reflection and the transmission are 0.7	No
This work	VO_2	Temperature, direction of the incident wave	① Transmission or reflection ② Efficiency ③ Janus MS feature	① Janus absorber ② PIT	① 1.448–2.497 THz ② 1.944–2.284 THz	Yes

provide a better understanding of the related work and show the MS's advantages in terms of functionality and adjustability.

3. Conclusions

In summary, we propose a Janus MS which is capable of switching from the PIT to absorption based on the anapole mode through adjustable materials VO_2. After conducting comprehensive theoretical simulations on various aspects, including the distribution of the surface currents, magnetic and electric fields, the scattering power intensity of multipole moments, and absorption, it was found that the MS produces a broadband PIT by coupling the localized plasmon resonance and the resonance employing NR as the bright plasmon resonator and CS as the quasi-dark mode plasmon resonator. This brings on a broad transparent window above 0.9, covering the frequency range from 1.944 THz to 2.284 THz when the VO_2 is inactive. An absorption peak of 0.921 is formed at 2.154 THz for the forward incident waves as the VO_2 functions. In terms of the backward incidence, it presents a broadband absorption covering 1.448–2.497 THz exceeding 0.9, which makes good use of the directionality peculiarity of the EM waves. It is worth highlighting that an ultra-broadband backward absorption from 0.7–10 Thz nearly all above 0.9 is provided as the incidence angle varies from 30°–70°. Moreover, the device possesses remarkable stability in polarization angles, and it can be extended beyond the THz region to other wavelength regions, including the microwave and even optical ranges. This proposal equipped with fabulous electric properties provides a path to create compact and versatile Janus devices,[64] showing great potential for various future applications, such as sensors with differential detection, multifunctional devices, and new digital MS-based information.

Conflicts of interest

There are no conflicts to declare.

References

1 B. Gerislioglu, A. Ahmadivand and N. Pala, *Phys. Rev. B*, 2018, **97**, 161405.
2 R. T. Ako, A. Upadhyay, W. Withayachumnankul, M. Bhaskaran and S. Sriram, *Adv. Opt. Mater.*, 2020, **8**, 1900750.
3 A. Ahmadivand, B. Gerislioglu, R. Ahuja and Y. K. Mishra, *Mater. Today*, 2020, **32**, 108.
4 J. B. Pendry, A. J. Holden, W. J. Stewart and I. Youngs, *Phys. Rev. Lett.*, 1996, **76**, 4773.
5 J. B. Pendry, A. J. Holden, D. J. Robbins and W. J. Stewart, *IEEE Trans. Microwave Theory Tech.*, 1999, **47**, 2075–2084.
6 T. Kim and C. Seo, *IEEE Microw. Wirel. Compon. Lett.*, 2000, **10**, 13–15.
7 A. K. Osgouei, H. Hajian, A. E. Serebryannikov and E. Ozbay, *J. Phys. D: Appl. Phys.*, 2021, **54**, 275102.
8 Y. Lv, D. D. Zhu, Y. J. Yin and H. F. Zhang, *Photonics Nanostructures – Fundam. Appl.*, 2023, **55**, 101136.
9 S. Khani and M. Afsahi, *Plasmonics*, 2023, **18**, 255–270.
10 N. Liu, L. Langguth, T. Weiss, J. Kstel, M. Fleischhauer, T. Pfau and H. Giessen, *Nat. Mater.*, 2009, **8**, 758.
11 Y. Huang, C. Min, P. Dastmalchi and G. Veronis, *Opt. Express*, 2015, **23**, 14922–14936.
12 S. Zhan, H. Li, Z. He, B. Li, Z. Chen and H. Xu, *Opt. Express*, 2015, **23**, 20313–20320.
13 Y. Liu, B. Li and Y. Xiao, *Nanophotonics*, 2017, **6**, 789–811.
14 X. L. Zhao, C. Yuan, L. Zhu and J. Q. Yao, *Nanoscale*, 2016, **8**, 15273–15280.
15 N. Papasimakis, V. A. Fedotov, V. Savinov, T. A. Raybould and N. I. Zheludev, *Nat. Mater.*, 2016, **15**, 263–271.

 This journal is © the Owner Societies 2023

16 Ia. B. Zel'Dovich, *Sov. Phys. JETP*, 1958, **6**, 1184–1186.
17 T. Kaelberer, V. A. Fedotov, N. Papasimakis, D. P. Tsai and N. I. Zheludev, *Science*, 2010, **330**, 1510–1512.
18 J. S. Totero Gongora, A. E. Miroshnichenko, Y. S. Kivshar and A. Fratalocchi, *Nat. Commun.*, 2017, **8**, 15535.
19 W. J. Luo, X. B. Wang, X. C. Chen, S. Y. Zheng, S. Q. Zhao, Y. Z. Wen, L. X. Li and J. Zhou, *Mater. Horiz.*, 2023, **10**, 1769–1779.
20 V. F. Gili, L. Carletti, A. Locatelli, D. Rocco, M. Finazzi, L. Ghirardini, I. Favero, C. Gomez, A. Lematre, M. Celebrano, C. De Angelis and G. Leo, *Opt. Express*, 2021, **29**, 11132.
21 P. G. De Gennes, *Angew. Chem., Int. Ed. Engl.*, 1992, **31**, 842–845.
22 C. Wan, C. Dai, S. Wan, Z. Li, Y. Shi and Z. Li, *Opt. Express*, 2021, **29**, 33954–33961.
23 P. Yu, J. Li, S. Zhang, Z. Jin, G. Schütz, C. Qiu, M. Hirscher and N. Liu, *Nano Lett.*, 2018, **18**, 4584–4589.
24 W. Tang, H. Zhang, H. Ma, W. Jiang and T. Cui, *Adv. Opt. Mater.*, 2019, **7**, 1800421.
25 R. Zhao, G. Lu, H. Yin, J. Liang, D. Zeng and H. Xiao, *Int. J. Antennas Propag.*, 2020, **2020**, 1–13.
26 Z. X. Wang, H. C. Zhang, J. Lu, P. Xu, L. W. Wu, R. Y. Wu and T. J. Cui, *J. Phys. D: Appl. Phys.*, 2018, **52**, 025107.
27 L. Shi, J. Shang, Z. Liu, Y. Li, G. Fu, X. Liu, P. Pan, H. Luo and G. Liu, *Nanotechnology*, 2020, **31**, 465501.
28 T. Deng, J. Liang, J. Lou, C. Zhang, Z. Du, C. Wang and T. Cai, *Opt. Express*, 2021, **29**, 7558–7567.
29 Y. Pang, Y. Li, J. Zhang, Z. Xu and S. Qu, *IEEE Antennas Wirel. Propag.*, 2018, **17**, 1123–1126.
30 F. Zhou, Y. Fu, R. Tan, J. Zhou and P. Chen, *Opt. Express*, 2021, **29**, 34735–34747.
31 W. Wan, Y. Li, H. Wang, Y. Cheng, Z. Zhu, H. Chen, W. Wang, L. Zheng, J. Wang and S. Qu, *IEEE Antennas Wirel. Propag.*, 2021, **20**, 1819–1823.
32 C. Wang, Y. Li, Y. Han, M. Feng, J. Wang, H. Ma, J. Zhang and S. Qu, *AIP Adv.*, 2018, **8**, 095211.
33 W. Jiang, Y. Fan, H. Ma, J. Wang, L. Yan, P. Han and S. Qu, *Phys. Lett. A*, 2020, **384**, 126103.
34 C. Wang, Y. Li, M. Feng, J. Wang, H. Ma, J. Zhang and S. Qu, *IEEE Trans. Antennas Propag.*, 2019, **67**, 6508–6514.
35 Z. Gao, Q. Fan, C. Xu, X. Tian, C. Tian, J. Wang and S. Qu, *Opt. Express*, 2021, **29**, 28767–28777.
36 Y. Shen, J. Zhang, Y. Meng, Z. Wang, Y. Pang, J. Wang, H. Ma and S. Qu, *Appl. Phys. Lett.*, 2018, **112**, 254103.
37 Y. Shen, J. Zhang, W. Wang, Y. Pang, J. Wang, H. Ma and S. Qu, *J. Phys. D: Appl. Phys.*, 2018, **52**, 085103.
38 Y. Pang, J. Wang, H. Ma, M. Feng, Y. Li and S. Qu, *Sci. Rep.*, 2016, **6**, 1–9.
39 Z. Zhu, Y. Li, J. Zhang, J. Wang, W. Wan, L. Zheng, M. Feng, H. Chen and S. Qu, *Opt. Express*, 2021, **29**, 4219–4229.
40 X. X. Liu, G. H. Yang, E. G. Tao, L. Q. Ma, Y. L. Lv and W. C. Shi, *IEEE*, Harbin, China, 2014, p. 1115.
41 Z. Shen, S. Li, Y. Xu, W. Yin, L. Zhang and X. Chen, *Phys. Rev. Appl.*, 2021, **16**, 014066.
42 G. P. Willeke and A. Räuber, *Semiconductors and Semimetals Elsevier*, 2012, vol. 87, pp. 7–48.
43 T. Matsumura, T. Nakatani and T. Yagi, *Appl. Phys. A*, 2007, **86**, 107.
44 Y. Z. Sun, Z. H. Guo, C. J. Gao and H. F. Zhang, *Phys. Scr.*, 2021, **96**, 12553.
45 S. Yuan, R. Yang, J. Tian and W. Zhang, *International Journal of RF and Microwave Computer-Aided Engineering*, 2020, vol. 30, p. e2201.
46 F. L. Zhang, X. C. Huang, W. Q. Cai, R. S. Yang, Q. H. Fu, Y. C. Fan, Y. J. Hu, K. P. Qiu, W. H. Zhang, C. Li and Q. Li, *Opt. Express*, 2020, **28**, 17481–17489.
47 Y. Z. Sun, C. J. Gao, J. Qu and H. F. Zhang, *Ann. Phys.*, 2022, **534**, 2200130.
48 M. D. Eisaman, A. André and F. Massou, *Nature*, 2005, **438**, 837–841.
49 C. J. Ma, Y. B. Zhang, Y. Zhang, S. Q. Bao, J. S. Jin, M. Li, D. M. Li, Y. G. Liu and Y. P. Xu, *Nanoscale Adv.*, 2021, **3**, 5636–5641.
50 H. G. Deng, L. L. Tian, R. J. Xiong, G. Liu, K. Yang, H. H. Zhao and W. H. Wang, *J. Cent. South Univ.*, 2020, **27**, 698–710.
51 A. A. Basharin, V. Chuguevsky, N. Volsky, M. Kafesaki and E. N. Economou, *Phys. Rev. B*, 2017, **95**, 035104.
52 X. Wang, M. Yan, Y. Fan, X. Fu, S. Qu, J. Wang, Y. Li, H. Chen, W. Chen, Q. Yuan and H. Ma, *J. Phys. D: Appl. Phys.*, 2019, **53**, 085001.
53 H. Pan, B. X. Li and H. F. Zhang, *Phys. Chem. Chem. Phys.*, 2023, **25**, 11375–11386.
54 G. Yang, F. Yan, X. Du, T. Li, W. Wang, Y. Lv, H. Zhou and Y. Hou, *AIP Adv.*, 2022, **12**, 045219.
55 H. Feng, Z. Zhang, J. Zhang, D. Fang, J. Wang, C. Liu, T. Wu, G. Wang, L. Wang and L. Ran, *Nanomaterials*, 2022, **12**, 1731.
56 Y. Cheng and J. Zhao, *Phys. Scr.*, 2022, **97**, 095508.
57 J. Zhao and Y. Cheng, *Adv. Theory Simul.*, 2022, 2200520.
58 N. Mou, B. Tang, J. Li, Y. Zhang, H. Dong and L. Zhang, *Materials*, 2021, **14**, 5708.
59 H. Zou and Y. Cheng, *Opt. Mater.*, 2019, **88**, 674–679.
60 M. Mao, Y. Liang, R. Liang, L. Zhao, N. Xu, J. Guo, F. Wang, H. Meng, H. Liu and Z. Wei, *Nanomaterials*, 2019, **9**, 1101.
61 K. Chen, G. Ding, G. Hu, Z. Jin, J. Zhao, Y. Feng, T. Jiang, A. Alù and C. W. Qiu, *Adv. Mater.*, 2020, **32**, 1906352.
62 Z. Zhang, D. Wen, C. Zhang, M. Chen, W. Wang, S. Chen and X. Chen, *ACS Photonics*, 2018, **5**, 1794–1799.
63 G. Shang, H. Li, Z. Wang, S. N. Burokur and X. Ding, *ACS Appl. Electron. Mater.*, 2021, **3**, 2638–2646.
64 M. A. Hernández-Acosta, H. Martínez-Gutiérrez, C. L. Martínez-González, C. R. Torres-SanMiguel, M. Trejo-Valdez and C. Torres-Torres, *Phys. Scr.*, 2018, **93**, 125801.